Journal of Power Sources 195 (2010) 7302–7315

Contents lists available at ScienceDirect

Journal of Power Sources

journal homepage: www.elsevier.com/locate/jpowsour

Numerical simulation and experimental validation of liquid water behaviors in a proton exchange membrane fuel cell cathode with serpentine channels

Anh Dinh Le [a], Biao Zhou [a,*], Huan-Ruei Shiu [b], Chun-I. Lee [b], Wen-Chen Chang [b]

[a] Department of Mechanical, Automotive & Materials Engineering, University of Windsor, ON, Canada, N9B 3P4
[b] Energy and Environment Research Laboratories, Industrial Technology Research Institute, Hsinchu 31040, Taiwan, ROC

ARTICLE INFO

Article history:
Received 23 February 2010
Received in revised form 25 May 2010
Accepted 26 May 2010
Available online 1 June 2010

Keywords:
PEMFC
VOF
Numerical validation
Liquid water
Experimental visualization

ABSTRACT

The volume-of-fluid (VOF) approach is one of the most promising methods of investigating water transport and water management in proton exchange membrane fuel cells (PEMFCs). A general PEMFC model combined with the VOF method has been developed by our group to simulate the mechanisms of fluid flows, mass and heat transport, and electrochemical reactions in a PEMFC, and it is necessary to validate the numerical model through experiments. In this paper, both the numerical model and an experimental visualization that can simulate the motion and transport behavior of liquid water in a cathode flow channel of a PEMFC are presented. Direct optical visualization is used in this work to capture the droplets' motions with high spatial and temporal resolutions. The numerical model and experimental setup have similar geometric dimensions and operating conditions, and the results of the experiment are in good agreement with numerical simulations. Moreover, the physics of droplet and liquid water behavior based on certain material and liquid properties and the operating conditions in the fuel cell channel are also addressed. This analysis also offers some basic understanding of the mechanism of liquid droplet dynamics in numerical and experimental studies of micro-fluidics.

1. Introduction

Proton exchange membrane fuel cells (PEMFCs) are considered to be promising alternative energy sources for automobile, industrial, and portable applications in the near future. A PEMFC is an electrochemical device composed of two electrodes and an electrolyte to convert stored chemical energy from reactant gases into electrical energy. The processes in a PEMFC, however, are very complex and involve flow dynamics, multi-phase, multi-component species transport, heat and mass transport, and electrochemical reactions that cannot easily be investigated in detail through experiments. Specifically, water management and flooding due to excess water in the porous media and drying out of the membrane have presented critical challenges for fuel cell design and optimization. Therefore, a large number of mathematical and simulation models of water transport and management based on computational fluid dynamics (CFD) approaches have been developed over the last decade for different purposes and in different ways. The most recent, comprehensive, and novel PEMFC models involve solving multi-phase transport (gas mixture–liquid water phases) coupled with fluid flows, mass and heat transport, and electrochemical reactions in all layers of the fuel cell in a three-dimensional (3D) computational domain. General 3D, multi-phase PEMFC models can be categorized into the following approaches: the multi-phase mixture model (M^2 model), the two-fluid model, and the volume-of-fluid (VOF) model [1]. The M^2 model introduces liquid water saturation as a volume fraction of liquid water, and the multi-phase mixture is essentially considered to be a single-phase fluid with a varying phase composition. The mixture in the M^2 model does not have separate liquid and gas phases, and the multi-phase flow is calculated with a mass-averaged mixture velocity. Wang and Cheng [2] are the pioneering authors who proposed the M^2 approach to fuel cell modeling. Later M^2 models were developed by Wang et al. [3,4], Mazumder and Cole [5], and Ju [6]. The general idea behind developing M^2 models is solving the two-phase channel flow based on the two-phase Darcy law, and the two-phase transport inside the porous media is assumed to be governed by the capillary effect between the liquid and gas phases. In these models, the mathematical governing equations and numerical algorithms are solved by commercial CFD software like Fluent®, Star-CD®, CFDRC®, etc.

Whereas the M^2 models deal with two-phase flow with a single fluid dynamics equation with averaged properties, the two-fluid models analyze the two-phase water transport by solving a separate set of mass and momentum equations for each phase. By introducing one more equation for liquid water in terms of the liquid saturation, the two-fluid model looks more physically realistic. Moreover, the phase transfer equilibrium between the liquid and gas phases is also taken into account to describe condensation and

* Corresponding author. Tel.: +1 519 253 3000x2630; fax: +1 519 973 7007.
E-mail address: bzhou@uwindsor.ca (B. Zhou).

0378-7753/$ – see front matter © 2010 Elsevier B.V. All rights reserved.
doi:10.1016/j.jpowsour.2010.05.045

Nomenclature

g	gravitational acceleration, m s^{-2}
P	pressure, Pa
S	the source term
s	volume fraction
t	time, s
u, v, w	velocities in X, Y, and Z directions, respectively, m s^{-1}

Greek symbols

ε	porosity
κ	surface curvature
τ_g	gaseous permeability, m^2
μ	dynamic viscosity, kg m^{-2} s^{-1}
ρ	density of gas mixture, kg m^{-3}
χ	surface tension coefficient, N m^{-1}
θ_w	contact angle

Subscripts

g	gas phase
i	species i
l	liquid phase

evaporation. Typical two-fluid models for two-phase transport in PEMFCs have been developed by Berning and Djilali [7], Ye and Nguyen [8], He et al. [9], Berning [10], and Gurau et al. [11]. In these models, the liquid water transport through the gas diffusion layers GDL, catalyst layers, and the membrane is modeled using viscous forces, gravity, and capillary pressure. Two-phase models are capable of describing the three-dimensional nature of the physical transport and distributions of two-phase flow, pressure, temperature, and species concentrations. Simulation results have shown that the presence of liquid water in the GDLs is strongly affected by the material properties (pore size, porosity), relative permeability, and capillary pressure of the porous media. However, the saturated permeability, relative permeability, and capillary pressure in diffusion medium are calculated differently in different models, and the accuracy of a model's results can be affected if the parameters of the simulation are incorrect.

Although multi-phase mixture and multi-fluid models account for two-phase transport with liquid and gas phases and introduce liquid water saturation as a liquid water volume fraction, these models are not capable of locating the presence of liquid water in terms of liquid droplets or water slugs locally concentrated, dispersed, or accumulated in the channels and porous media. Thus, the formation and motion of liquid water cannot be observed on the scales studied in experimental investigations. To overcome these limitations, Zhou et al. developed a powerful approach to dealing with liquid water behavior in the cathodes of single PEMFCs or fuel cell stacks by incorporating the volume-of-fluid (VOF) technique to track the dynamic air–water interface [12–16]. The results showed that differences in GDL design significantly affect the liquid water flow patterns, thus influencing the performance of PEMFCs. Detailed liquid water flow patterns and droplet motion and removal were also shown in these works. Following the work of Zhou et al., two-phase flow models incorporating the VOF algorithm to study characteristics of liquid water behavior in the flow channels and/or GDLs were developed by Djilali and co-workers [17–19], Zhan et al. [20], Cai et al. [21], and Golpaygan and Ashgriz [22]. These models, however, do not account for the electrochemical reactions, heat and mass transport, and phase change processes in practical PEMFCs. Despite including the VOF technique to investigate the dynamic behavior of two-phase flow, these models eliminate the "source" of water vapor and the phase change process that transforms water vapor to liquid or liquid to vapor. Furthermore, these models do not consider the effects of liquid water on physical and electrochemical transport. With further improvements, Le and Zhou [23–25] have developed a general PEMFC model that includes the electrochemical reactions, fluid dynamics, and transport processes along with the VOF technique for solving the two-phase problems. The aim of this general PEMFC model is to understand the motion of liquid water and its effects on the performance of fuel cells, so liquid water was supplied by water injection to shorten the computing time.

Although the VOF method is considered to be one of the most effective ways to model PEMFCs, it is necessary to validate the numerical model and computational algorithm through experiments. Numerical predictions can be considered reliable and accurate if the numerical model is well-resolved and has been systematically validated against carefully obtained experimental data. Hence, experimental investigations of liquid water transport in a PEMFC are taken into account for the purpose of comparison. To date, most investigations of liquid water behavior in PEMFCs have been conducted using various imaging visualization techniques [26]. The direct optical visualization technique has been used to observe the formation of liquid water and subsequent transport in the channels of transparent fuel cells [27–32] or at the surface of the gas diffusion layer (GDL) [33]. The optical method is capable of operating at time intervals as low as milliseconds per frame and at various length scales from channel size (in mm-scale) to the scale of porous media void regions (in μm-scale). Despite the advantages mentioned above, the most significant disadvantage of optical visualization is that it is unable to capture invisible water in the liquid or vapor phase in the flow channels or inside of the porous media layers. To overcome the limitations of the optical method, the neutron imaging technique has recently been employed in the literature [34–42]. Using neutron radiographs to detect the invisible water in opaque objects is well suited to observing the transport properties of the water inside the GDLs and the membranes of PEMFCs. In contrast to the optical technique, the neutron imaging technique has average resolution in time and space and requires expensive modern equipment such as neutron sources. Another technique similar to neutron imaging is magnetic resonance imaging (MRI), which can detect and visualize liquid water under the gas channels and collector ribs of PEMFCs [43–46]. Each method mentioned above has advantages and disadvantages, and in general, they each play a significant role in understanding water management in PEMFCs and investigating the effects of water transport on fuel cell performance.

In this study, in addition to the VOF numerical model, an experimental visualization of the motion and transport behavior of liquid water in the cathode flow channel of an experimental PEMFC, has been developed. Direct optical visualization was used, as it can capture the droplets' motions and liquid water distribution with high spatial and temporal resolutions. The numerical model of the fuel cell is set up on a computational domain with the same geometric dimensions and operating conditions as the experimental fuel cell setup. The experimental data are used to qualitatively and quantitatively validate the results of the VOF numerical model.

2. Description of experimental devices and setup

The experimental system is composed of an experimental PEMFC cathode, a fuel cell test bench (including air supply tanks, flow controllers, flow and pressure transducers, and data acquisition systems—DAQs), and a commercial camera supported with optical lenses and a light source as shown in Fig. 1.

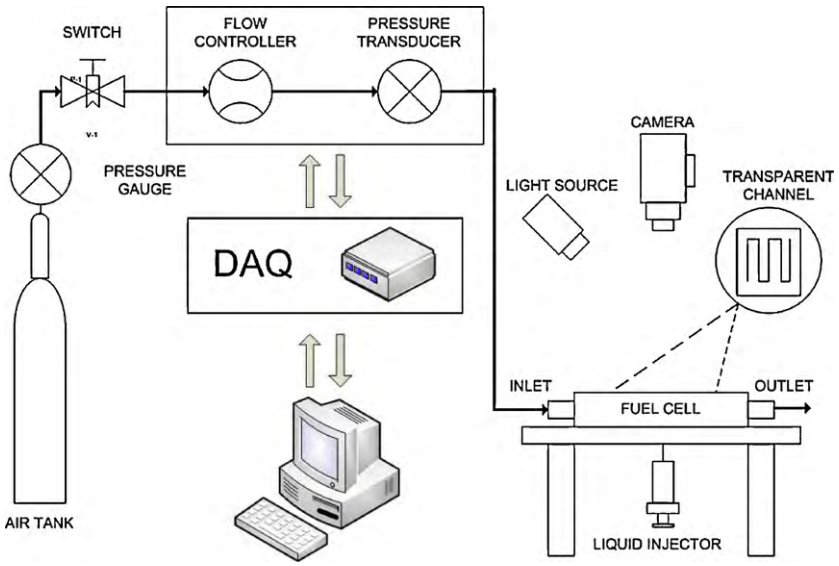

Fig. 1. Schematic diagram of fuel cell experimental visualization system.

The experimental system is operated as follows: a series of liquid water droplets under various air flow conditions are injected into the flow channel via a liquid injector to visualize the temporal evolution of the liquid transport process. The motion and deformation of each droplet are captured by the camera, which will export the visualized data to the computer as a movie file. The operating conditions in the flow controller, such as the air flowrate, are set via control signals sent from the computer via the DAQ hardware. The output parameters, such as inlet and outlet pressures, are obtained from pressure transducers and monitored by the computer through self-developed code in the LABVIEW® software environment [47]. The characteristic length of the experiment is on the order of microns and the characteristic time scale is on the order of μs. The experimental visualization was focused on validating the numerical results by identifying the lengths and shapes of droplets and liquid water and the characteristic of the liquid motion.

2.1. Droplet generation

A number of droplets were injected into the channel via the needle of a liquid injector placed under the fuel cell cathode channel and porous media (membrane electrode assembly (MEA)). By applying force to the plunger, liquid water was pushed out of the cylindrical tube on demand, as shown in Fig. 2. The fluid volume initially oscillates upon injection and creates spherical droplets at the point of the needle, as this configuration minimizes the interface energy (i.e., the surface tension effect). The velocities and shapes of the droplets are dependent on the force applied to the plunger, the environment in which the droplets are created, and the diameters and dimensions of the plunger, the cylindrical tube, and the needle.

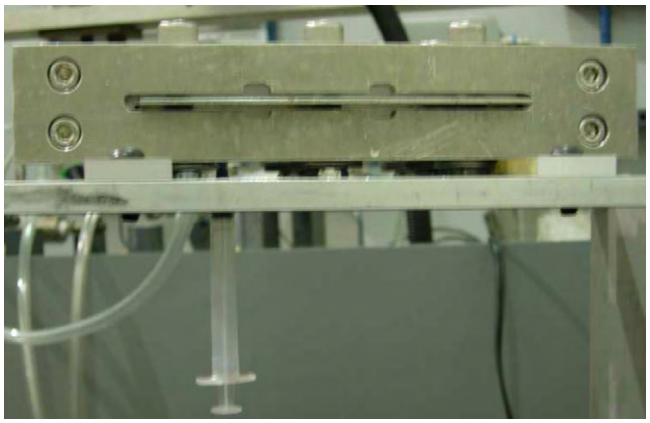

Fig. 2. Droplet generation in the experimental visualization.

This experimental work uses hypodermic needles with an inner diameter of 400 μm. The working fluid is dyed liquid water. The preliminary droplet created at the needle tip in an atmospheric environment without convection (no air flow) has a maximum diameter of 3.4 mm as calculated by the volume measurement method. As calculated under the operating conditions of the experiment, the droplet diameter is approximately 1 mm at an air flow inlet velocity of 5.9 m s^{-1}.

2.2. Properties of the water droplet

2.2.1. Contact angle of the droplet

Contact angle is one of the most important factors affecting liquid transport in fuel cell channels and porous media. By definition, the contact angle is the angle at which a liquid/vapor interface meets the solid surface. Different types of liquid/gas interaction and different solid materials create different contact angles. In this experiment, we used a simple optical method to measure the contact angle of a water drop in different solid materials used in the experimental fuel cell. The values of the contact angle for different materials are shown in Table 1.

2.2.2. Surface tension

Because the portion of the dye in the liquid water is insignificant (approximately 1 g l^{-1}), the surface tension of the droplet is considered to be the surface tension of liquid water measured at the

Table 1
The values of contact angle of the droplet.

Liquid type	Solid materials	Location of solid surface	Contact angle (°)
Dyed water	Glass	Transparent plate—up wall	43
Dyed water	MEA	12E-W MEA—surface	130
Dyed water	Stainless steel	Collector/channel side wall	53

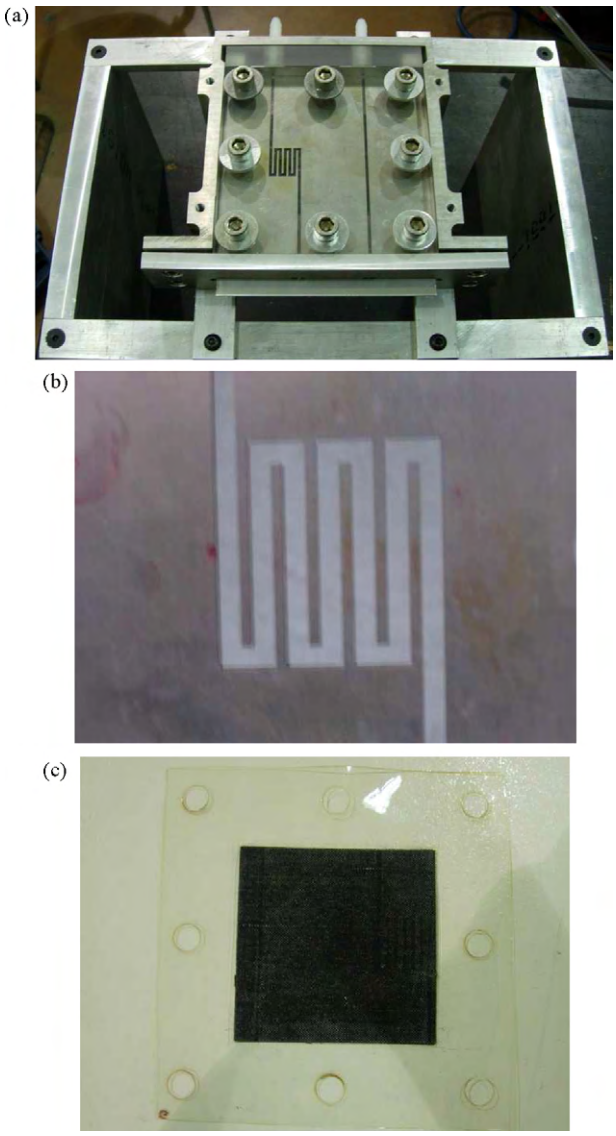

Fig. 3. (a) Structure of the transparent PEMFC cathode, (b) structure of the serpentine flow channel, and (c) structure of the 12E-W MEA.

operating temperature. The value of the surface tension at 20 °C is 0.072 N m^{-1}.

2.2.3. Viscosity

The liquid water viscosity was chosen to be 0.001003 kg m^{-1} s^{-1} at 25 °C. If the liquid water is dyed, then the viscosity is slightly different. However, the difference is negligible, as there is only a very small amount of dye dissolved in the pure liquid solution.

2.3. Experimental fuel cell design

The experimental PEMFC cathode assembly used in the experimental visualization is shown in Fig. 3a. The flow channel used in the experiment is serpentine (Fig. 3b) and was fabricated in a 1.7 mm thick stainless steel plate. The channel is 2 mm wide and 180 mm long. The plate was placed on a 12E-W MEA made by BASF® with an active area of 70 mm × 70 mm (Fig. 3c). To capture the motion of liquid water in the channel and connect the fuel cell cathode assembly, the steel plate and MEA were sandwiched between two plastic end plates, which were fixed by eight bolts distributed around the plates' edges. The channel inlet was also connected to the air gas feed from a fuel cell test bench by a flexible hose and the channel outlet was vented to atmosphere.

2.4. Visualization method

The direct optical visualization method is used to capture the liquid motion in a transparent PEMFC cathode. This method is quite sensitive and has high spatial and temporal resolutions when observing a flow field with velocities on the order of meters per second. In some cases, a high-speed camera is required, as pictures must be recorded at an acquisition rate of a thousand frames per second. The frame resolution, however, is inversely proportional to the frame rate, which may affect the quality of the recorded pictures. In this experimental work, temporal resolution was only required on the order of tens of μs, and a few seconds of pictures of liquid motion were captured to validate the numerical results. The commercial camera JVC GZ-MG 37 was utilized to visualize the liquid motion. The obtained movie files were processed in a PC and exported to picture files at a frame rate of 30 frames per second (fps), or a time resolution of 1/30 s (approximately 34 μs). The frame resolution was 640 × 480. During the recording process, microscope mode was employed to magnify the droplet images.

3. Description of numerical model setup

3.1. Methodology description

Fluid flow transport processes in the PEMFC are mathematically described by a set of conservation laws for mass and momentum transport. The gas and liquid phases are considered to be a two-phase mixture. To treat two-phase transport, including the liquid and gaseous phases, the water vapor is treated as a gaseous species in the species transport equations and the liquid water is tracked by using the volume fraction equation. The appropriate equations are numerically solved in the cathode channel and porous media with various source terms to produce a set of solutions describing the air and liquid flow in the computational domain.

3.1.1. Mass conservation equation

The mass (continuity) equation is expressed as follows:

$$\frac{\partial \varepsilon \rho}{\partial t} + \nabla(\varepsilon \rho \vec{v}) = S_m \quad (1)$$

The transient term represents the change of mass with time and the second term represents the change in mass flux; this is also known as the convection term. The velocity and density of the flow mixture, including the gaseous and liquid phases, are considered to be a variable and a property in the continuity equation, respectively. When the VOF method that will be described in the next section is employed, the volume fractions of different phases in the mixture are defined. The variables and properties are shared by the phases and defined by a volume-averaging calculation, as the volume fractions of the liquid phase s_l and gas phase s_g are known. The density in each computational cell is then [48]:

$$\rho = s_l \rho_l + s_g \rho_g \quad (2)$$

where ρ is the mixture density, which is considered to be the volume-averaged density of the liquid phase density ρ_l and the gas phase density ρ_g. By definition, the sum of the volume fractions of each phase in the mixture is unity.

$$s_l + s_g = 1 \quad (3)$$

3.1.2. Momentum conservation equation

A single momentum equation is solved throughout the domain, and the resulting velocity field is shared by the gas and

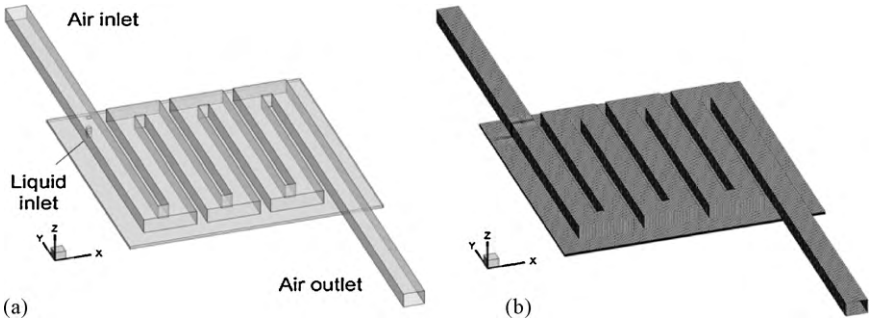

Fig. 4. (a) Schematic diagram and (b) computational mesh of the numerical model.

liquid phases [48],

$$\frac{\partial}{\partial t}(\varepsilon\rho\vec{v}) + \nabla(\varepsilon\rho\vec{v}\vec{v}) = -\varepsilon\nabla p + \nabla[\varepsilon\mu\nabla\vec{v}] + S_v \quad (4)$$

In the momentum equation, the transient term represents the change of momentum with time, and the second term describes the advection momentum flux. The first two terms on the right hand side of the momentum equation represent the change of momentum due to pressure and viscosity, respectively. The mixture properties are dependent on the volume fraction of each phase. The mixture viscosity μ is defined as

$$\mu = s_l\mu_l + (1 - s_l)\mu_g \quad (5)$$

Gravitational effects are taken into account in the source terms of the momentum equation. The other source terms are added in the different layers of the porous media to describe the flow of the fluid through a porous zone by using viscous loss, or the Darcy drag force. The use of Darcy's law to represent the source terms of the momentum equation in porous media is valid because the flow is laminar and viscous with very low velocity. The source terms are different in different regions of the fuel cell. In the flow channel, only the gravitational force is considered. However, the viscous loss (the Darcy drag force), the surface tension, and gravity are taken into account in the GDLs and catalyst layers. In the membrane, the source term that accounts for the electrokinetic permeability is added.

For flow channels,

$$S_v = \underbrace{\rho\vec{g}}_{\text{Gravity force}} \quad (6)$$

For porous media,

$$S_v = \underbrace{\rho\vec{g}}_{\text{Gravity force}} - \underbrace{\frac{\mu}{\tau_g}\varepsilon^2\vec{v}}_{\text{Darcy force}} + \underbrace{\chi\kappa\frac{2\rho\nabla s_l}{(\rho_l+\rho_g)}}_{\text{Surface tension force}} \quad (7)$$

where ε is the porosity of the porous media, κ is curvature, and τ_g is the permeability of the porous media (for each zone, such as the membrane, GDL or catalyst layer).

3.1.3. Volume fraction equation of liquid

The interface between the phases was tracked by using the VOF method to solve a continuity equation for the volume fraction of one of the phases of the two-phase model

$$\frac{\partial}{\partial t}(\varepsilon s_l\rho_l) + \nabla(\varepsilon s_l\rho_l\vec{v}_l) = S_{s_l} \quad (8)$$

The motion of the interface between the gas and liquid of different densities and viscosities was defined by the volume fraction of liquid water s_l and the volume fraction of the gaseous phase s_g [48]. Eq. (8) was employed to track the volume of the liquid phase, and it was solved over the entire domain. The source term of the volume fraction equation is considered to be zero, as there are no phase changes taken into account in this model.

3.2. VOF model

To solve for the two-phase transport in this model, the VOF technique was applied to the PEMFC model to track the movement of the interfaces and boundaries of liquid water in the mixture to explicitly investigate the transport and behavior of liquid water. Following this method, each phase of the two-phase flow can be represented by a single variable: the volume fraction of the phase in the computational cell volume. The model also includes the effects of surface tension and wall adhesion along the interfaces between the gas and liquid phases.

3.2.1. Geometric reconstruction scheme

The geometric piecewise linear interface construction (PLIC) scheme was chosen because it is more accurate and applicable to general unstructured meshes than other methods such as the donor–acceptor, Euler explicit, and implicit schemes. Basically, the VOF geometric reconstruction scheme is divided into two parts: the reconstruction step and the propagation step. More details describing this approach can be found in [48].

3.2.2. Implementation of surface tension

Surface tension is added to the VOF method in the source term of the momentum equation. The pressure drop across the surface depends on the surface tension coefficient χ

$$\Delta p = \chi\kappa = \chi\left(\frac{1}{R_1} + \frac{1}{R_2}\right) \quad (9)$$

where χ denotes the surface tension coefficient, κ is the surface curvature, and R_1 and R_2 are the two radii, in orthogonal directions, that measure the surface curvature. The surface tension force can be written in terms of the pressure difference across the interface, which is expressed as a volumetric force F that is added to the momentum equation

$$\vec{F} = \chi\kappa\frac{\rho\nabla s_l}{(\rho_l+\rho_g)/2} \quad (10)$$

The term $\rho/((\rho_1+\rho_2)/2)$ is used to improve the capability of the continuum surface force (CSF) method for modeling surface tension in the presence of fine meshes at high-density ratio interfaces. This method is called "density-scaling of the CFS", and it helps to maintain a constant interface thickness when tracking the interface between a dense phase (namely, liquid water) and a light phase (namely, air) using the VOF algorithm [49]. The surface curvature κ can be defined in terms of the divergence of the normal unit vector of the interface $\hat{n}$

$$\kappa = \nabla\hat{n} = \nabla(\hat{n}_{SS}\cos\theta_{SS} + \hat{t}_{SS}\sin\theta_{SS}) \quad (11)$$

Table 2
The geometrical dimension and physical properties of three different meshes.

Case no.	Inlet air flow-rate ($kg\,s^{-1}$)	Inlet liquid flow-rate ($kg\,s^{-1}$)	Number of grid cells in the channel cross-section	Grid size in the channel (mm)	Number of grid cells in the domain
1	2e−5	1.65e−5	6 × 6	0.333	26,984
2	2e−5	1.65e−5	12 × 12	0.166	160,768
3	2e−5	1.65e−5	18 × 18	0.055	408,780

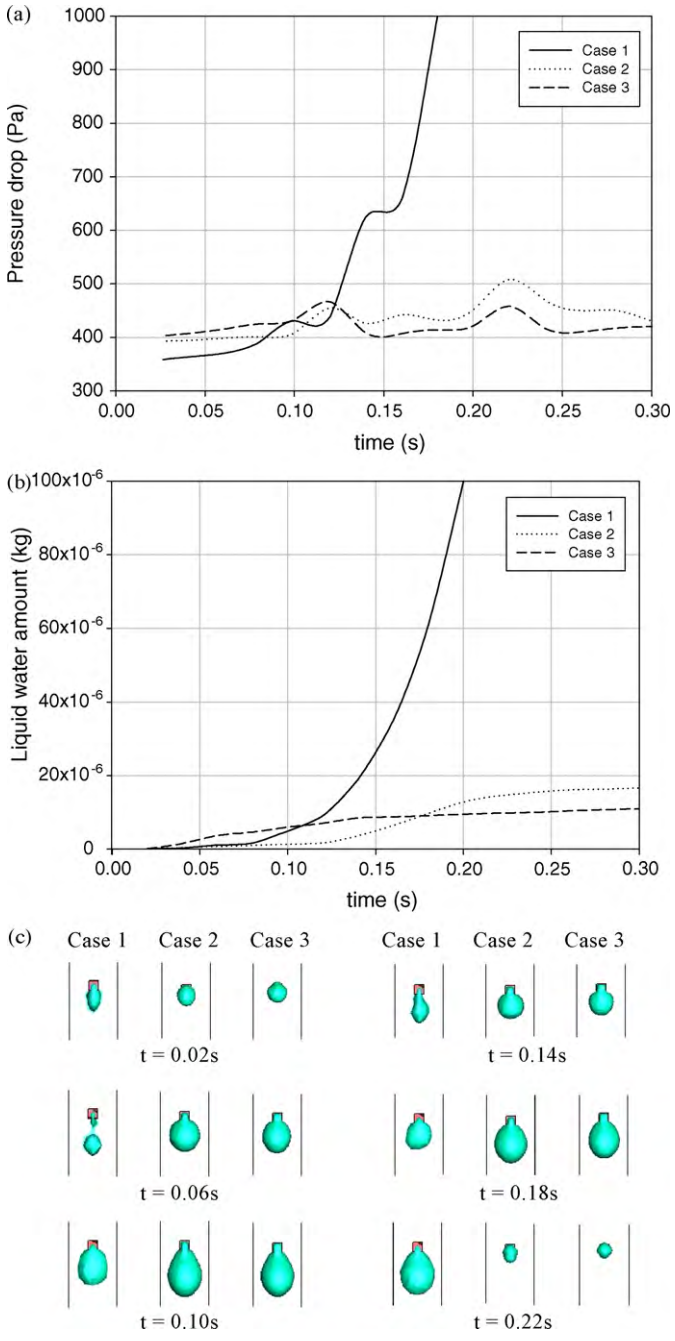

Fig. 5. Grid dependency: (a) pressure drop, (b) liquid water amount, and (c) droplet deformation at needle point, in the channel for the three cases with different grid sizes.

where $\hat{n}$ is the unit vector normal to the interface between the two phases near the solid surfaces, $\hat{n}_{SS}$ is the unit vector normal to the solid surfaces, $\hat{t}_{SS}$ is the unit vector tangential to the solid surfaces, and θ_{SS} is the static contact angle at the solid surfaces. Different static contact angles can be assigned to electrode surfaces with different wettabilities, leading to different surface tensions ($\vec{F}$) and influencing water transport.

3.3. Numerical algorithm

3.3.1. Computational domain and numerical procedure

The computational domain of the fuel cell used for the numerical model was set up with the same geometrical dimensions as the cell used in the experiment, which consists of a MEA, a cathode flow channel, and a collector plate, as shown in Fig. 4. The computational grids were implemented with 285,168 grid cells by the Gambit® 2.3 mesh generation software package and solved using Fluent® 6.3. The number of computational cells in the cross-sectional area of the channel was 12 × 12. The VOF algorithm was incorporated along with a flow field solver to investigate the behavior of liquid water in the channel. The Pressure-Based Segregated Solver incorporated in the SIMPLE algorithm [50] was implemented in a parallel computing setup, and the solution was considered to have converged when the residual criteria reach a value accurate on the order of 10^{-4}.

3.3.2. Validation of grid independency

To ensure that the grid resolution is sufficient to resolve the physical scales of the model and does not significantly affect the calculation time, the solution was checked at different grid sizes, and a range of grid sizes in which the solutions are reasonably independent on the size of grid was obtained. In this study, three serpentine channel meshes with different grid sizes were examined with the geometry and flow conditions shown in Table 2. In Fig. 5, the pressure drops and amounts of liquid water in the channel for the three cases are examined and compared. The numerical simulation shows that Case 1, with a coarse grid, resulted in an unreliable pressure drop and amount of liquid. In Case 2 and Case 3, the deformation and injection time of droplets were grid-dependent, and the scales of the pressure drop and amount of water were on the same order for the two cases. Although the results from Case 2 and Case 3 at a certain time were not identical, the major features did not change significantly. Therefore, the numerical simulation used Case 2 to reduce the calculation time but produce an adequate solution.

Table 3
Operating condition and physical properties of the experiment and numerical model.

Parameters	Value
Inlet gas flow-rate	$2 \times 10^{-5}\,kg\,s^{-1}$
Inlet liquid flow-rate	$1.65 \times 10^{-5}\,kg\,s^{-1}$
Operating temperature	20 °C
Surface tension	$0.072\,N\,m^{-1}$
Contact angle of the transparent glass	43°
Contact angle of the collector/channel plate	53°
Contact angle of the MEA	130°
Air viscosity at 20 °C	$1.7894 \times 10^{-5}\,kg\,m^{-1}\,s^{-1}$
Liquid water viscosity at 20 °C	$0.001003\,kg\,m^{-1}\,s^{-1}$

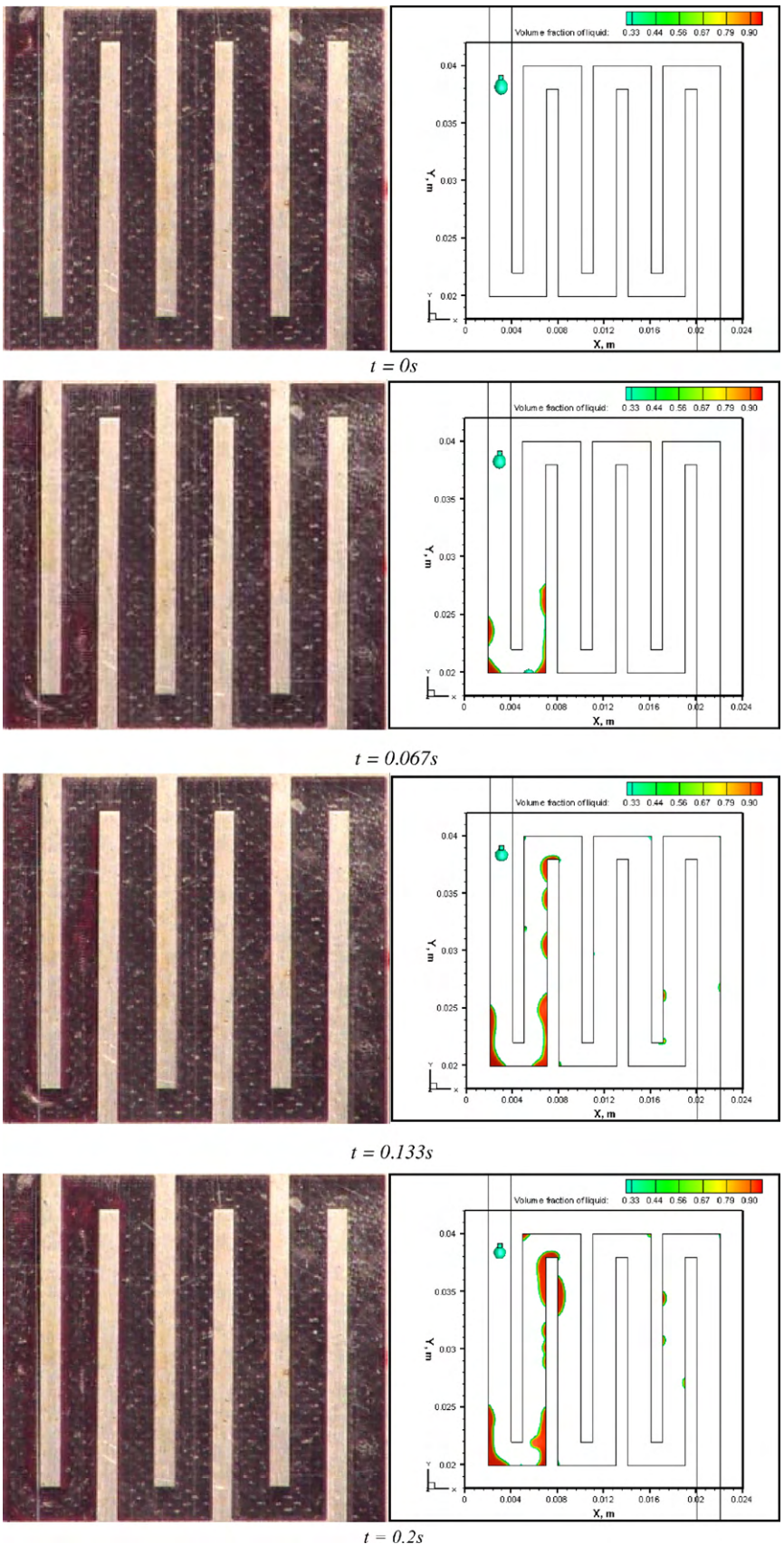

Fig. 6. Visualization of liquid motion in the channel at different time steps.

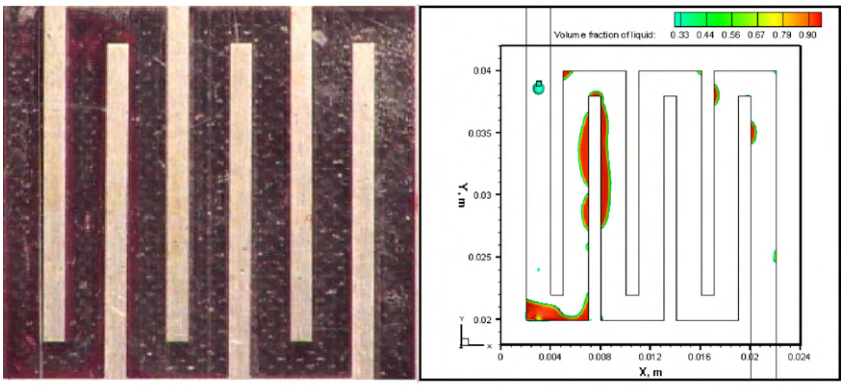

t = 0.267s

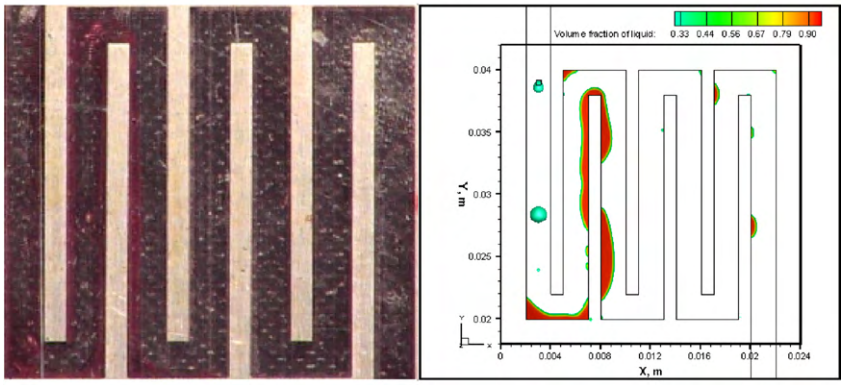

t = 0.333s

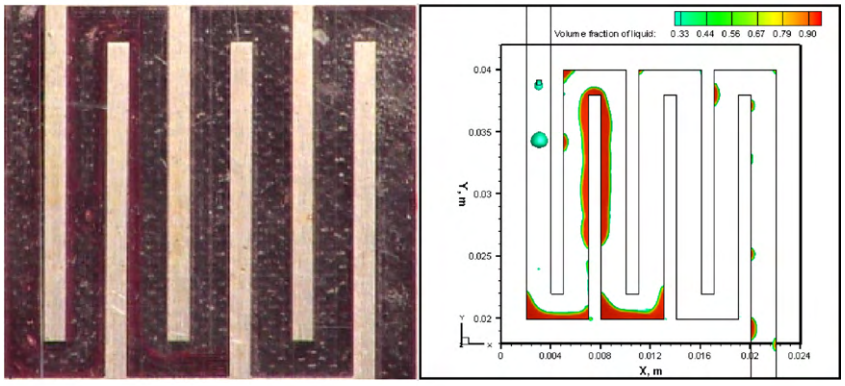

t = 0.4s

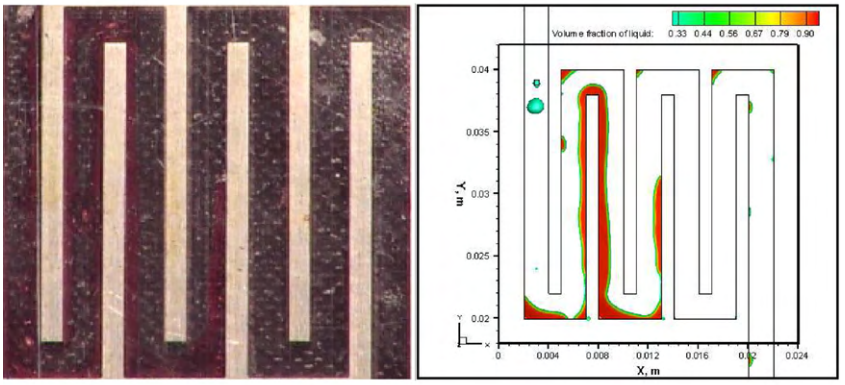

t = 0.467s

Fig. 6. (*Continued*)

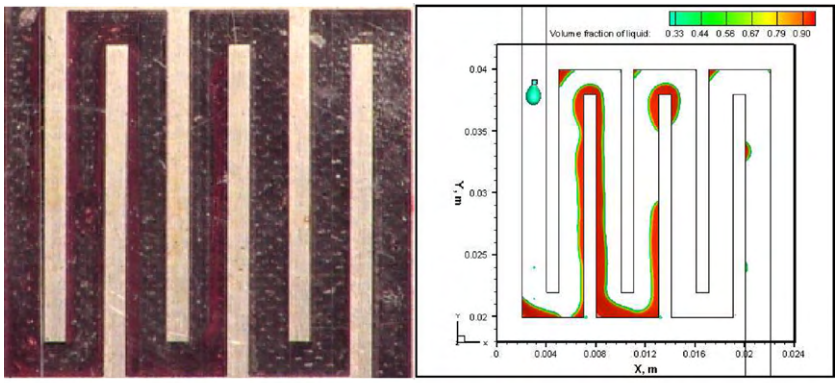

t = 0.533s

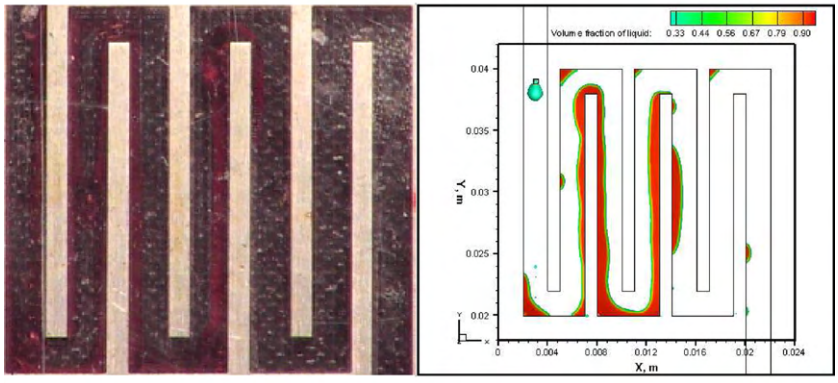

t = 0.6s

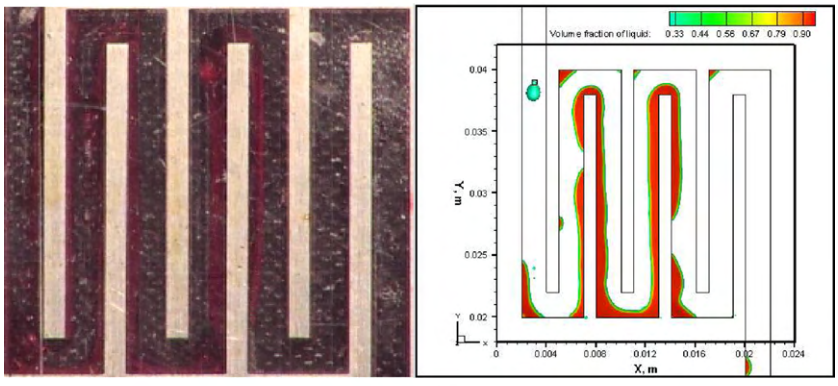

t = 0.667s

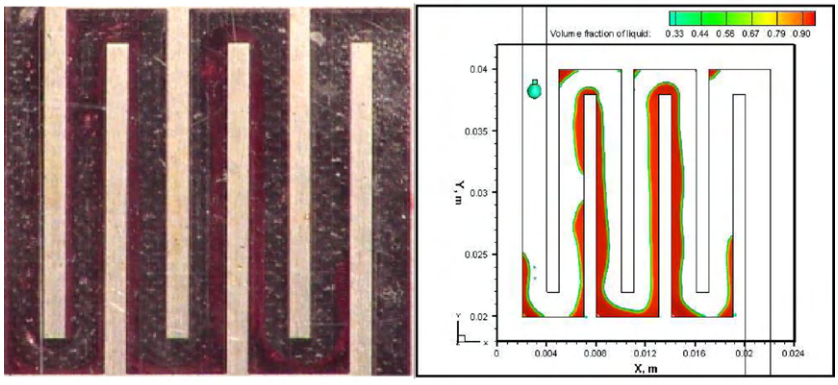

t = 0.733s

Fig. 6. (*Continued*)

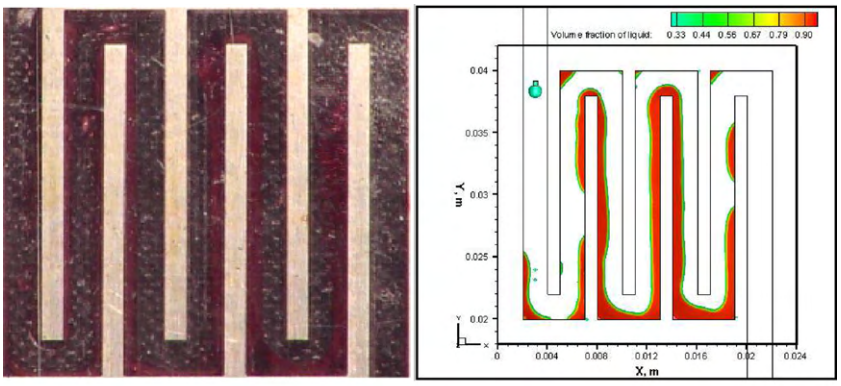

t = 0.8s

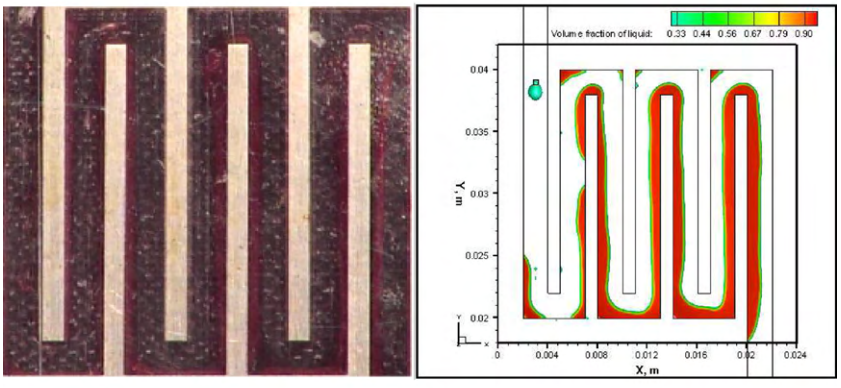

t = 0.867s

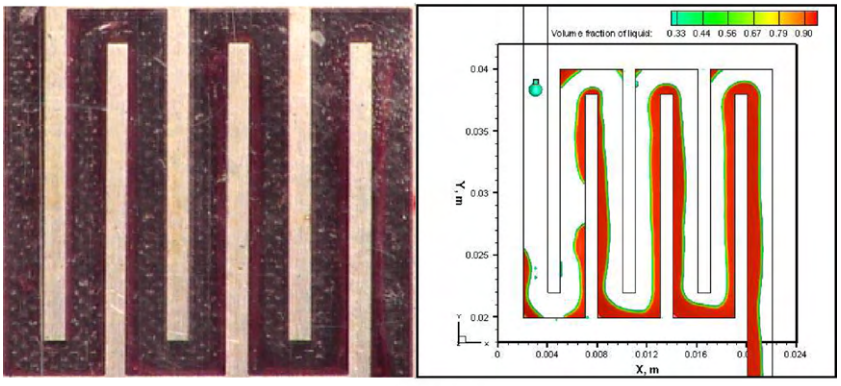

t = 0.933s

Fig. 6. (*Continued*).

4. Results and discussion

4.1. Operating conditions and physical properties

To compare with experiment and validate the numerical results, the experiment and numerical model were set up with the same operating conditions for fluid flow and material properties, shown in Table 3.

To set the physical fluid flow and material properties, these parameters were measured in the experiment and then used in the numerical model. The inlet gas flow-rate was measured by a flow-rate controller on the fuel cell test bench. The liquid flow-rate was measured by the "Bucket-and-stopwatch" method. The liquid flow-rate was measured in the experiment by examining displacement of a volume of liquid water moving in the syringe over a certain time period.

4.2. Dimensionless number

To compare the experimental and numerical results and examine the physics of liquid flow dynamics under the same operating conditions in both cases, the dimensionless Reynolds (Re), Weber (We) and Bond (Bo) numbers were determined as follows:

Reynolds number: The Reynolds number of the air flow represents the ratio of the inertial force to the viscous force and is defined as

$$Re = \frac{UD_h}{\nu} \tag{12}$$

where U is the air flow velocity, D_h is the hydraulic diameter of the channel, and ν is the kinematic viscosity of air. Because the inlet air flow velocity in the channel was 5 ms^{-1} and the hydraulic diameter of the rectangle channel was 0.0018 m [51], the Reynolds number

is

$$Re = \frac{5 \times 0.0018}{1.6 \times 10^{-5}} = 562.5 \quad (13)$$

Weber number: The Weber number is considered to be the ratio between inertia and surface tension. It explains how significantly the surface tension force affects the droplet behavior. It can be expressed as

$$\mathrm{We} = \frac{\rho V^2 L}{\chi} \quad (14)$$

where V is the velocity of the droplet (assumed to be the air velocity when the liquid is in motion in the air flow field), ρ is the density of liquid water, L is the characteristic length (the contact radius of the droplet), and χ is the surface tension.

Bond number: The Bond number is defined as the ratio between the gravitational force and the surface tension force.

$$\mathrm{Bo} = \frac{\Delta \rho g R^2}{\chi} \quad (15)$$

where $\Delta\rho$ is the difference between the density of the liquid and the density of the surrounding fluid, g represents the gravitational

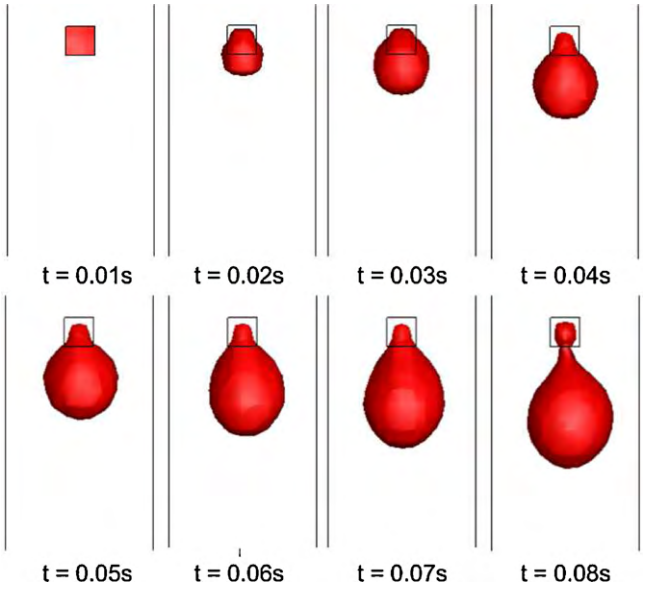

Fig. 7. Development of pendant droplet in the channel.

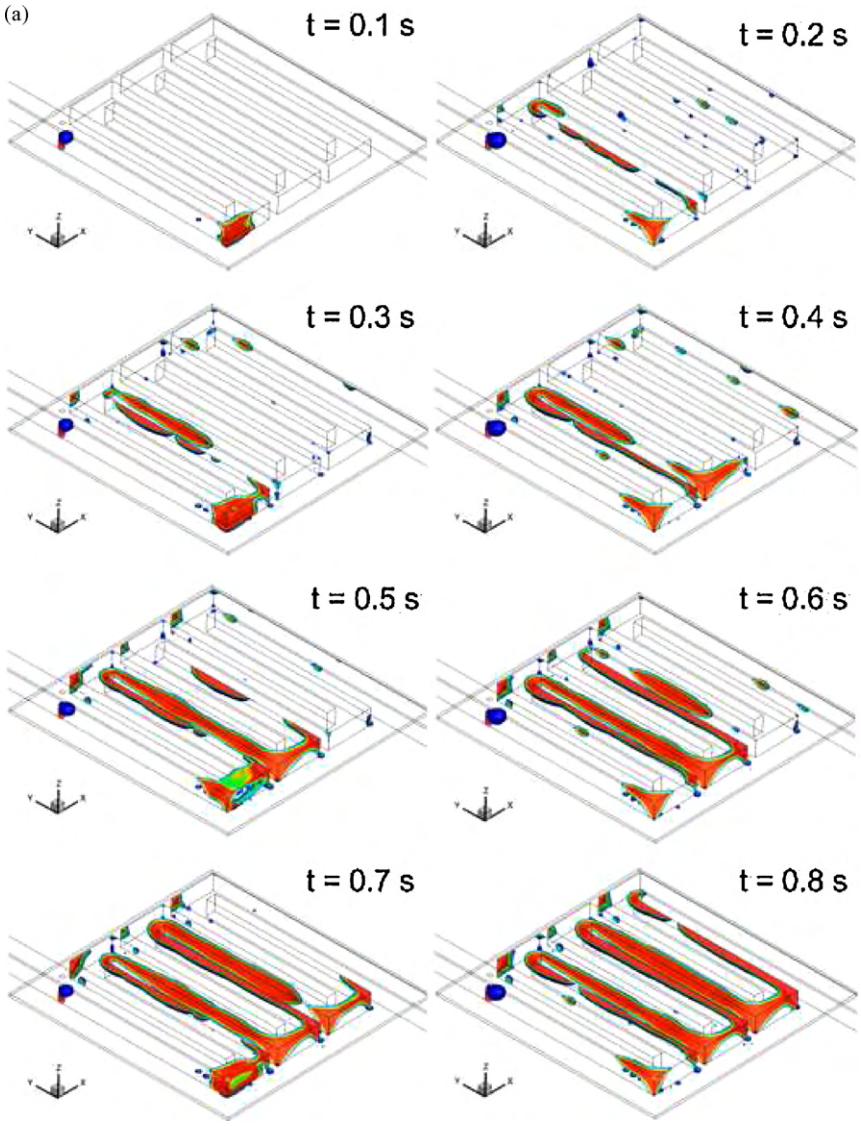

Fig. 8. Development of flattened droplet in the channel: (a) from top view and (b) from bottom view.

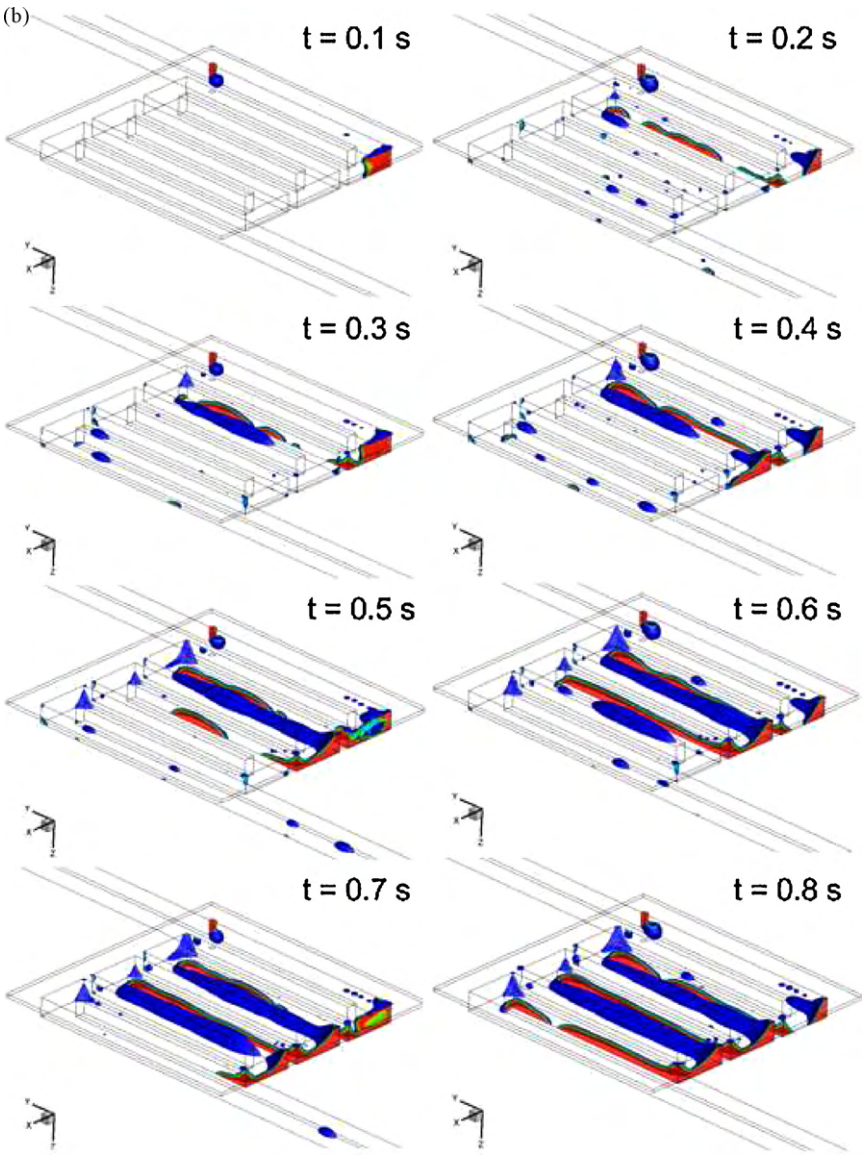

Fig. 8. (*Continued*).

acceleration, χ is the surface tension, and R is the typical dimension of the droplet.

4.3. Experimental and numerical visualizations of liquid water motion in the channel—comparison and analysis

4.3.1. Model comparison

Fig. 6 shows a comparison of the experimentally measured and numerically simulated liquid droplet motion in the serpentine channel of a fuel cell under the operating conditions listed in Table 3. The processes were visualized over 1 s, which is sufficient to describe and investigate the motion and behavior of the liquid water at any instant from the beginning, when the liquid is injected into the channel, to the end, when the liquid water is removed from the channel by the air-flow field. In Fig. 6, the liquid water in the channel is dyed red in the experiment. The series of images in Fig. 6 show that the experimental visualization and numerical simulation provide comparable results, with similar droplet shapes and spatial-temporal positions of liquid water in the channel.

4.3.2. Physics of the droplets and liquid motion

The droplets are injected into the channel via the needle placed inside. When a drop appears at the point of needle, it is deformed by the shearing force from the air flow field and takes on a pendant shape. This drop is called a "pendant drop" [52]. The shape of the droplet is determined by the Weber number, which is the ratio between inertia and surface tension. In other words, the inertial force tends to elongate the droplet along the flow direction, whereas the surface tension force tends to minimize the interface by making the droplet spherical. Fig. 7 shows the time evolution of the droplet deformation, with a Weber number and a Bond number that are calculated as

$$\mathrm{We} = \frac{1000 \times 5^2 \times 0.0007}{0.072} = 243 \tag{16}$$

$$\mathrm{Bo} = \frac{(1000 - 1) \times 9.81 \times 0.0007^2}{0.072} = 0.067 \tag{17}$$

Obviously, based on the Weber and Bond numbers, it can be concluded that the droplet shape is mainly governed by the inertial

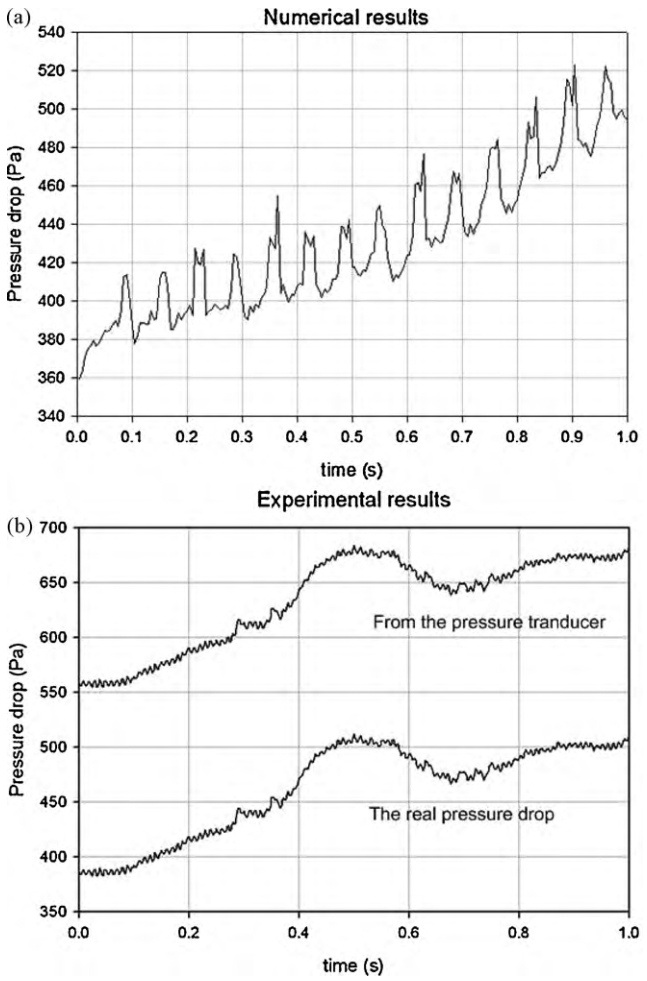

Fig. 9. Comparison of pressure drop in the channel under the presence of liquid water.

force rather than by the surface tension force in the *Y* direction. Note that, the effect of gravity can only be considered in the *Z* direction (normal to the *X*–*Y* plane).

Under shearing stress from the air flow, the droplet is deformed and then detached from the needle point. It moves along the direction of the air flow and hits the wall at the turn in the channel due to its inertia. After hitting the wall, as shown in Fig. 8, the liquid interfaces in contact with the solid wall tend to spread to the corners between two different solid walls (sidewall and top wall for the transparent glass, or sidewall and bottom surface for MEA). In Fig. 8, the volume fractions of the liquid are indicated by the color, which varies from blue ($s_l = 0.2$) to red ($S_l = 1$). The contact angles of different walls are different, and the shapes of droplets are dependent on the values of these contact angles. This phenomenon is also known as the Concus–Finn relation, described in [52]; the liquid droplet tends to spread into a corner when the contact angles of the surfaces are small (hydrophilic materials), and it tends to be spherical, without wetting the tip of the corner, when the contact angles of the surfaces are large (hydrophobic materials). Because liquid droplets are continuously provided to the channel from the needle, a stretched liquid forms along the channel from $t = 0.1\ s$ to $t = 0.8\ s$, as shown in Fig. 8. The formation of the droplet shape in the channel can be explained by several factors: the inertial force due to the air flow moving in the channel, the contact angles of the walls that form the channel, and the geometry of the channel. If shearing stress is caused by strong air flow, then the liquid droplet tends to be widely flattened. In other words, the liquid droplet is driven by the shearing stress from the air flow field. The liquid droplets always move along a side of the channel wall, even in the regions where the channel turns. The second factor is the contact angle, which follows the Concus–Finn relation. One of three morphologies (filament, wedge, or droplet) is formed depending on the contact angle. Filaments are formed if the contact angles are smaller than 45°, and stretched droplets or droplets are formed if the contact angles are larger than 45°. Structures that are nearly filamentary occur in the corner between the upper wall (transparent glass) with a contact angle of 43° and the side wall (stainless stain plate) with a contact angle of 53°.

4.3.3. Qualitative comparison between the numerical and experimental models by evaluating the pressure drop in the channel

The numerical and experimental results are validated through a quantitative comparison of the pressure drop in the channel. Fig. 9 shows values of the pressure drop in the channel while liquid drops are being continuously injected into the channel over 1 s. The pressure drop indicates the difference between the pressures at the inlet and outlet of the channel. The pressure drop increases as time progresses and more and more liquid droplets appear in the channel. Although liquid water is continuously added to the channel by the constant liquid flow-rate from the syringe, the rate of appearance of liquid droplets at the needle point is not constant. Recall that liquid water does not stream out of the needle point into the channel. Actually, a liquid droplet is formed, gradually grows, and is removed due to the shearing force from the air flow. After that, another droplet is formed, and the process continues. Obviously, this process is discontinuous. The pressure drop increases as a droplet is formed and decreases when the droplet is removed. This leads to the pressure oscillations observed in Fig. 9. The differences in pressure drop over 1 s in the numerical simulation and experiment are of similar orders of magnitude. However, the pressure indicated in the experimental pressure transducer is higher than that indicated in the numerical simulation, because the position of the pressure sensor in the experiment is not the same as the position at which the inlet pressure is calculated in the numerical model. It is necessary to account for the pressure drop in the manifold, the hose connected to the fuel cell inlet, and the extra channel used to connect the fuel cell to the fuel cell test bench. The pressure drops in the manifold, the connected hose, and the extra channel are calculated by using Darcy's formulation [51] for laminar flow

$$\Delta P_L = f\frac{L}{D}\frac{\rho V_{\text{avg}}^2}{2} \tag{18}$$

For the manifold,

$$\Delta P_1 = \frac{64}{Re}\frac{L}{D}\frac{\rho V_{\text{avg}}^2}{2} = \frac{64}{562.5}\frac{0.1}{0.002}\frac{1.125 \times 5.2^2}{2} = 86.5\ \text{Pa} \tag{19}$$

For the extra channel,

$$\Delta P_2 = \frac{57}{Re}\frac{L}{D}\frac{\rho V_{\text{avg}}^2}{2} = \frac{57}{562.5}\frac{0.07}{0.0018}\frac{1.125 \times 5.2^2}{2} = 60\ \text{Pa} \tag{20}$$

For the connected hose, the pressure drop is measured to be approximately 20 Pa. Thus, the total pressure drop due to the connection is approximately 167 Pa. Subtracting this pressure drop from the pressure drop measured by the pressure transducer in the experiment, we obtain the actual experimental value of the pressure drop in the channel. Fig. 9 shows that the scale of this pressure drop is similar to that obtained from the numerical results.

5. Conclusions

Experimental visualization of droplet motion in the cathode channel was developed to validate a numerical simulation that uses

the VOF model and to investigate the physics of liquid droplets in a cathode of PEMFC. The experimental devices and setup, including an experimental PEMFC, a liquid injection system, an optical camera, and a light source, were used to observe liquid motion in the channel over a short period of time. The experimental data were then analyzed and compared with the results of numerical simulation. The geometric dimensions, material properties, and operating conditions were the same in the experimental setup and the numerical model, to allow for comparison. The main conclusions can be summarized as follows:

- The shapes and locations of the droplet at a given time in the numerical model and the experiments are in good agreement. The pressure drop in the channel and the pressure rise due to liquid injection were also examined in both cases. The similarity of the pressure scale and pressure changes ensures that the operating conditions used in the simulation model and the experiments were identical and reasonable. Hence, it can be concluded that the general, 3D, numerical PEMFC model using the VOF method for multi-phase flows is suitable for investigating the physical and transport phenomena in PEMFCs.
- The physics of the droplet and liquid water transport in a fuel cell channel were also investigated. The results show that the shapes of the droplets and the behavior of the liquid water were quite similar to results described in previous studies with similar liquids, material properties, and operating conditions. The key factors that determined the shapes and behaviors of the droplets were the velocity of the air flow, the contact angle, the surface tension, and the viscosity of the droplet.

References

[1] H. Wu, X. Li, P. Berg, Electrochimica Acta 54 (2009) 6913–6927.
[2] C.Y. Wang, P. Cheng, International Journal of Heat Mass Transfer 39 (1996) 3607–3618.
[3] Y Wang, S. Basu, C.Y. Wang, Journal of Power Sources 179 (2008) 603–617.
[4] S. Basu, J. Li, C.Y. Wang, Journal of Power Sources 187 (2009) 431–443.
[5] S. Mazumder, J.V. Cole, Journal of the Electrochemical Society 150 (11) (2003) A1510–A1517.
[6] H. Ju, Journal of Power Sources 185 (2008) 55–62.
[7] T. Berning, N. Djilali, Journal of the Electrochemical Society 150 (12) (2003) A1589–A1598.
[8] Q. Ye, T.V. Nguyen, Journal of the Electrochemical Society 154 (12) (2007) B1242–B1251.
[9] G. He, P. Ming, Z. Zhao, A. Abudula, Y. Xiao, Journal of Power Sources 163 (2007) 864–873.
[10] T. Berning, ECS Transactions 16 (2) (2008) 23–34.
[11] V. Gurau, T.A. Zawodzinski, J.A. Mann, Journal of Fuel Cell Science and Technology 5 (2008), 021009-1.
[12] P. Quan, B. Zhou, A. Sobiesiak, Z. Liu, Journal of Power Sources 152 (2005) 131–145.
[13] K. Jiao, B. Zhou, P. Quan, Journal of Power Sources 154 (2006) 124–137.
[14] K. Jiao, B. Zhou, P. Quan, Journal of Power Sources 157 (2006) 226–243.
[15] K. Jiao, B. Zhou, Journal of Power Sources 169 (2007) 296–314.
[16] K. Jiao, B. Zhou, Journal of Power Sources 175 (2008) 106–119.
[17] X. Zhu, P.C. Sui, N. Djilali, Journal of Power Sources 172 (2007) 287–295.
[18] X. Zhu, P.C. Sui, N. Djilali, Microfluidics & Nanofluidics 4 (6) (2008) 1613.
[19] X. Zhu, P.C. Sui, N. Djilali, Journal of Power Sources 181 (2008) 101–115.
[20] Z. Zhan, J. Xiao, M. Pan, R. Yuan, Journal of Power Sources 160 (2006) 1–9.
[21] Y.H. Cai, J. Hu, H.P. Ma, B.L. Yi, H.M. Zhang, Journal of Power Sources 161 (2006) 843–848.
[22] A. Golpaygan, N. Ashgriz, International Journal of Computation Fluid Dynamics 22 (2008) 85–95.
[23] A.D. Le, B. Zhou, Journal of Power Sources 182 (2008) 197–222.
[24] A.D. Le, B. Zhou, Electrochimica Acta 54 (2009) 2137–2154.
[25] A.D. Le, B. Zhou, Journal of Power Sources 193 (2009) 665–683.
[26] A. Bazylak, International Journal of Hydrogen Energy 34 (2009) 3845–3857.
[27] K. Tuber, D. Pocza, C. Hebling, Journal of Power Sources 124 (2003) 403–414.
[28] Z. Liu, Z. Mao, C. Wang, Journal of Power Sources 158 (2006) 1229–1239.
[29] D. Spernjak, A.K. Prasad, S.G. Advani, Journal of Power Sources 170 (2007) 334–344.
[30] S. Ge, C.Y. Wang, Journal of the Electrochemical Society 154 (10) (2007) B998–B1005.
[31] E. Kimball, T. Whitaker, Y.G. Kevrekidis, J.B. Benziger, AIChE Journal 54 (5) (2008) 1313–1332.
[32] D Spernjak, S.G. Advani, A.K. Prasad, Journal of the Electrochemical Society 156 (1) (2009) B109–B117.
[33] B. Gao, T.S. Steenhuisa, Y. Zevi, J.Y. Parlangea, R.N. Carter, T.A. Trabold, Journal of Power Sources 190 (2009) 493–498.
[34] T.A. Trabold, J.P. Owejan, D.L. Jacobson, M. Arif, P.R. Huffman, International Journal of Heat and Mass Transfer 49 (2006) 4712–4720.
[35] J.P. Owejan, T.A. Trabold, D.L. Jacobson, D.R. Baker, D.S. Hussey, M. Arif, International Journal of Heat and Mass Transfer 49 (2006) 4721–4731.
[36] I. Manke, Ch. Hartnig, M. Grünerbel, J. Kaczerowski, W. Lehnert, N. Kardjilov, A. Hilger, J. Banhart, W. Treimer, M. Strobl, Applied Physics Letters 90 (2007) 184101.
[37] M.A. Hickner, N.P. Siegel, K.S. Chen, D.N. McBrayer, D.S. Hussey, D.L. Jacobson, M. Arif, Journal of the Electrochemical Society 153 (2006) A902–A908.
[38] M.A. Hickner, N.P. Siegel, K.S. Chen, D.S. Hussey, D.L. Jacobson, M. Arif, Journal of the Electrochemical Society 155 (2008) B294–B302.
[39] M.A. Hickner, N.P. Siegel, K.S. Chen, D.S. Hussey, D.L. Jacobson, M. Arif, Journal of the Electrochemical Society 155 (4) (2008) B427–B434.
[40] J.B. Siegel, D.A. McKay, A.G. Stefanopoulou, D.S. Hussey, D.L. Jacobson, Journal of the Electrochemical Society 155 (11) (2008) B1168–B1178.
[41] J. Park, X. Li, D. Tran, T. Abdel-Baset, D.S. Hussey, D.L. Jacobson, M. Arif, International Journal of Hydrogen Energy 33 (2008) 3373–3384.
[42] C. Hartnig, I. Manke, R. Kuhn, S. Kleinau, J. Goebbels, J. Banhart, Journal of Power Sources 188 (2009) 468–474.
[43] S. Tsushima, K. Teranishi, S. Hirai, Electrochemical and Solid-State Letters 7 (2004) A269–A272.
[44] K.R. Minard, V.V. Viswanathan, P.D. Majors, L.Q. Wang, P.C. Rieke, Journal of Power Sources 161 (2006) 856–863.
[45] D. Zachary, R.I. Masel, Journal of Power Sources 171 (2007) 678–687.
[46] J. Bedeta, G. Maranzana, S. Leclerc, O. Lottin, C. Moyne, D. Stemmelen, P. Mutzenhardt, D. Canet, International Journal of Hydrogen Energy 33 (2008) 3146–3149.
[47] J. Chen, B. Zhou, Journal of Power Sources 177 (2008) 83–95.
[48] Fluent® 6.3 Manual, Fluent Inc., 2006.
[49] D.B. Kothe, W.J. Rider, S.J. Mosso, J.S. Brock, J.I. Hochstein, AIAA (1996), 96-0859.
[50] S.V. Patankar, Numerical Heat Transfer and Fluid Flow, Hemisphere Publ. Corp, 1980.
[51] Y.A. Cengel, J.M. Cimbala, Fluid Mechanics—Fundamentals and Applications, 1st ed., McGraw-Hill, 2006.
[52] J. Berthier, Microdrops and Digital Microfluidics, William Andrew, New York, 2008.